Nanoscale

ROYAL SOCIETY OF CHEMISTRY

PAPER

View Article Online
View Journal | View Issue

Cite this: *Nanoscale*, 2021, **13**, 20299

Minimized thermal expansion mismatch of cobalt-based perovskite air electrodes for solid oxide cells†

Zhishan Li, [a] Meilan Peng,[a] Yingru Zhao,[a] Jianhui Li [b] and Yifei Sun *[a,c,d]

The mismatch of thermal expansion coefficients (TECs) between cobalt-containing perovskite air electrodes and electrolytes is a great challenge for the development of thermo-mechanically durable solid oxide cells (SOCs). In this work, we propose a facile design principle to directly grow highly dispersed Co reactive sites onto ion-conducting scaffolds and confine the dimension of active centres within nanoscale. As a representative, the Co-socketed $BaCe_{0.7}Zr_{0.2}Y_{0.1}O_{3-\delta}$ perovskite (denoted as R-BCZY-Co) was constructed *via* a consecutive sol–gel and *in situ* exsolution approach. Combined XRD, H_2-TPR, SEM and TEM results confirm the emergence of Co nanoparticles on a BCZY matrix without the segregation of a secondary Co-rich phase. The symmetric half-cell measurement suggests that R-BCZY-Co air electrode with the optimal Co content of 10 mol% exhibits a 7-fold promoted oxygen activation performance with a polarization resistance of ~0.17 Ω cm^2 at 750 °C. The TEC mismatch between fabricated R-BCZY-Co electrodes and BCZY electrolytes is minimized down to only ~11.4%, which is significantly lower than that of other representative counterparts. Moreover, the detailed XPS result proves that the architecture of exsolved Co on BCZY possesses a higher concentration of surface oxygen vacancy, which further benefits the kinetics of ion diffusion and oxygen absorption.

Received 16th October 2021,
Accepted 15th November 2021

DOI: 10.1039/d1nr06845h

rsc.li/nanoscale

1 Introduction

Solid oxide cell (SOC), having the modes of fuel cell (SOFC) and electrolysis cell (SOEC), is a kind of reversible energy conversion device with high efficiency, which has attracted much attention from various research communities.[1,2] The conventional oxygen ion–conducting SOC (O-SOC) is using yttrium-doped zirconia oxide (YSZ) as an electrolyte, which usually operate at high temperatures (800–1000 °C). Typically, O-SOC has desirable stability but restricted choice of electrode materials.[3] In comparison, the proton-conducting SOC (H-SOC) could operate at intermediate temperatures (500–750 °C), showing advantages of lower activation energy for ionic transportation and higher electrode flexibility.[4]

Currently, cobalt-containing perovskites are the most widely investigated air electrodes for SOCs.[5–8] However, the huge mismatch in thermal expansion coefficients (TECs) between air electrodes and electrolytes is still the biggest issue hindering the commercialization of SOCs.[9] For example, the TECs of representative proton-conducting electrolytes, BZCY ($BaZr_{0.1}Ce_{0.7}Y_{0.2}O_{3-\delta}$) and BCZYYb ($BaCe_{0.7}Zr_{0.1}Y_{0.1}Yb_{0.1}O_{3-\delta}$), were measured to be in the range of 9–13 × 10^{-6} K^{-1},[3,10] while Co-based air electrode materials such as $La_{0.6}Sr_{0.4}Co_{0.2}Fe_{0.8}O_{3-\delta}$ (LSCF) and $Ba_{0.5}Sr_{0.5}Co_{0.8}Fe_{0.2}O_{3-\delta}$ (BSCF) obtain TECs falling in the range of 20–25 × 10^{-6} K^{-1}.[11,12] The greater TEC of Co-based perovskites is due to the larger radius of Co ions after thermal reduction (Co^{4+}, 0.068 nm; Co^{3+}, 0.075 nm; Co^{2+}, 0.088 nm) and spin state transition.[13] Such huge discrepancy of TECs results in the delamination at electrode/electrolyte interfaces and internal stress of cells, significantly reducing the thermo-mechanical stability.[9] A previous study disclosed that approximately 10% of interface area would suffer from delamination when the difference in TEC between electrode and electrolyte reached 7 × 10^{-6} K^{-1}.[14]

So far, various strategies have been developed to deal with this challenge. The cobalt-containing perovskites were directly

[a]*College of Energy, Xiamen University, Xiamen, Fujian, 361102, China. E-mail: yfsun@xmu.edu.cn*
[b]*National Engineering Laboratory for Green Chemical Productions of Alcohols, Ethers and Esters, College of Chemistry and Chemical Engineering, Xiamen University, Xiamen, Fujian, 361005, China*
[c]*Shenzhen Research Institute of Xiamen University, Shenzhen, Guangdong, 518057, China*
[d]*State Key Laboratory of Physical Chemistry of Solid Surfaces, College of Chemistry and Chemical Engineering, Xiamen University, Xiamen, Fujian, 361005, China*
†Electronic supplementary information (ESI) available. See DOI: 10.1039/d1nr06845h

mixed with electrolyte powders as the electrode composites to reduce the TECs.[15–17] On the other hand, the defect engineering in the perovskite structure[18] and the construction of cobalt-free multiphase nanocomposite[19] were also reported to reduce the TECs of the air electrode. However, these results are still not perfectly satisfactory. Zhang *et al.* proposed a novel thermal-expansion offset strategy that a negative-thermal-expansion component ($Y_2W_3O_{12}$) was introduced to eliminate the TEC mismatch of Co-based perovskite ($SrNb_{0.1}Co_{0.9}O_{3-\delta}$) with the electrolyte ($Sm_{0.2}Ce_{0.8}O_{1.9}$, SDC).[9] Even so, other alternative methods without introducing the secondary phase are still highly worthy of pursuing in the perspective of reduced system complexity and uncertainty.

In decade, the *in situ* exsolution of cation to metal in reducing condition at elevating temperature has emerged as a hot research topic for functional perovskite oxide design.[20–25] Such approach endows the strong metal–oxide interface, improved agglomeration resistance and high element utilization efficiency, which is practical for the application of electrochemical/heterogeneous catalysis including solid oxide cells.[25]

Enlightened by this conception, herein, we demonstrate a design paradigm to manufacture the *in situ* exsolved Co active site–socketed BCZY heterostructure, which realizes the promotion of catalytic activity, manipulation of overall TEC of electrode and minimization of the mismatch with electrolyte, simultaneously. The Co element was preliminarily doped into the lattice of BCZY perovskite and then exsolved out as nanoparticles (NPs) evenly anchored on the surface of porous scaffold. As a result, the as-obtained composite electrode shows 7-fold enhancement in the electrochemical performance with the negligible TEC mismatch of only ~11.4%. This study offers a new thinking for robust SOC electrode design, which has promising generality to be employed in other cell systems.

Yifei Sun

Dr Yifei Sun is an Associate Professor in the College of Energy, Xiamen University, China. He received his bachelor and master degrees in Chemistry from Xiamen University. Then, he pursued his PhD degree in Chemical engineering from the University of Alberta, Canada. After accomplishing his postdoctoral career at Purdue University, USA, he joined Xiamen University as a faculty by the end of 2019. His current research focused on the design, development and understanding of functional oxide materials, especially perovskite oxides, toward electrochemistry, heterogeneous catalysis, and various energy conversion systems. He also has particular interest in the application exploration of perovskite oxide for multidisciplinary fields such as neuromorphic computing.

2 Experimental

2.1 Synthesis of electrode powders

The BCZY electrolyte and a series of Co-doped Ba$(Ce_{0.7}Zr_{0.2}Y_{0.1})_{1-x}Co_xO_{3-\delta}$ (denoted as BCZY-Co_x, x = 0.025, 0.05, 0.075, 0.10, 0.15 and 0.20) powders were synthesized by the sol–gel method described elsewhere.[26,27] For BCZY, stoichiometric amounts of metal nitrates $Ba(NO_3)_2$ (Sinopharm Chemical Reagent, 99.5%), $Ce(NO_3)_3{\cdot}6H_2O$ (Energy Chemical, 99.99%), $Zr(NO_3)_2{\cdot}5H_2O$ (Energy Chemical, 99.9%) and $Y(NO_3)_3{\cdot}6H_2O$ (Energy Chemical, 99.99%) were dissolved in deionized water. The solution was heated to 40 °C under stirring. Then, metal nitrate, citric acid (CA, Macklin Reagent, 99.5%) and ethylenediaminetetraacetic acid (EDTA, Macklin Reagent, 99.5%) were added in molar ratios of 1 : 1.5 : 1. The pH value of this mixture was adjusted to ~8 with ammonium hydroxide ($NH_3{\cdot}H_2O$, Sinopharm Chemical Reagent, 25–28%). The mixture was subsequently heated to 80 °C under stirring until the solvent was vaporized and a viscous gel was formed. Afterward, the gel was heated to 170 °C for 10 h to form a sponge-like material. The resulting material was grounded and compacted into pellets, and then calcined at 1100 °C for 5 h to avoid barium volatilization.[28] Similarly, BCZY-Co_x was synthesized with additional $Co(NO_3)_2{\cdot}6H_2O$ (Energy Chemical, 98%) added. The resulting mixture was also compacted into pellets and calcined at 1100 °C for 5 h to obtain BCZY-Co_x powders. After reduction at 800 °C for 10 h in an atmosphere containing 5% H_2/N_2, the *in situ* exsolved Co-decorated BCZY-Co_x powders (denoted as R-BCZY-Co_x) were synthesized.

2.2 Fabrication of the symmetric half-cells

The dense BCZY electrolyte was prepared by the dry-pressing method. Approximately 0.5 g BCZY, 1 wt% NiO (Aladdin Reagent, 99%) and an appropriate amount of polyvinyl alcohol (PVA, Aladdin Reagent, M_w of ~145 000) were mixed thoroughly and then pressed in a stainless-steel module with a diameter of ~18.0 mm. The mixture was sintered at 1450 °C for 10 h in air atmosphere to densify the electrolyte. The diameter and thickness of the obtained BCZY electrolyte were ~14.7 and ~0.4 mm, respectively. The sintering shrinkage of the electrolyte was calculated to be ~18.3%, indicating that the electrolyte is dense enough.

The symmetric half-cells of BZCY-Co_x||BCZY||BZCY-Co_x were fabricated by the screen printing method.[29,30] First, a slurry of BCZY-Co_x was prepared by thoroughly mixing an electrode powder and a screening glue at a weight ratio of 1 : 1.5. The glue was composed of ~7 wt% ethyl cellulose (Acmec, Viscosity of ~180–220) in terpineol (Xilong Chemical, AR), and an appropriate amount of butyldigol (Xilong Chemical, AR) was added to adjust the viscosity. Second, the electrode slurry was screen-printed on the two sides of BCZY electrolyte with

an active area of ~0.5 cm^2 and subsequently sintered at 1100 °C for 5 h in air atmosphere. After reduction at 800 °C for 10 h in an atmosphere containing 5% H_2/N_2, the obtained half-cells were denoted as R-BZCY-Co_x||BCZY||R-BZCY-Co_x. The BCZY||BCZY||BCZY symmetric half-cell was also fabricated as a reference by screen-printing a pure BCZY slurry on the two sides of BCZY electrolyte. Finally, the Ag paste was painted onto the surface of electrode as a current collector and Ag wires were used as current collectors to connect the symmetric half-cell with the electrochemical workstation (Wuhan Corrtest Instruments, CS2350H). Ag wires were fixed to the Ag paste using a silver conducting resin (Shanghai Institute of Synthetic Resin, DAD87).

2.3 Electrochemical characterization

Electrochemical impedance spectroscopy (EIS) measurement was carried out on R-BZCY-Co_x||BCZY||R-BZCY-Co_x (x = 0.025, 0.05, 0.075, 0.10, 0.15 and 0.20) symmetric half-cells to estimate the electrochemical performance of R-BZCY-Co_x as air electrode for SOC. The performance of BCZY||BCZY||BCZY symmetric half-cell was measured as a reference. The half-cell was heated from room temperature to 750 °C at a ramping rate of 3 °C min^{-1}, and then its EIS data were obtained at 750, 700, 650, 600 and 550 °C in air under open-circuit voltage (OCV) condition and the frequency ranging from 10^5 to 0.01 Hz with a potential amplitude of 10 mV using a CS2350H electrochemical workstation.

For the van der Pauw DC conductivity test, the electrode slurry was screen-printed on only one side of BCZY electrolyte with an active area of ~0.5 cm^2, followed by calcination at 1100 °C for 5 h in air atmosphere. Four Ag wires were mounted on the surface of electrode layer by introducing four contact points with an inscribed square formed. The calculation of electrode conductivity was reported in the literature.[31]

2.4 Physicochemical characterization

The phase structure of BCZY electrolyte, BZCY-Co_x and R-BZCY-Co_x air electrode powers was determined by an X-ray diffractometer (XRD, Rigaku Ultima IV) equipped with a Cu Kα radiation source (40 kV, 30 mA) in the 2θ interval from 10° to 90° with a scanning rate of 8° min^{-1}. The *in situ* exsolved Co NPs on R-BCZY-Co_x powders were analysed by high-resolution slow step scan XRD (2θ = 43–46°, the scanning rate of ~1° min^{-1}). The hydrogen temperature-programmed reduction (H_2-TPR) was performed using a home-made chemisorption apparatus equipped with a thermal conductivity detector (TCD) to detect H_2 consumption. Approximately 0.1 g BZCY-Co_x sample was pre-treated by 5% H_2/N_2 at room temperature for 1.5 h and then heated to 850 °C at a ramping rate of 5 °C min^{-1}. The morphology of exsolved Co NPs on R-BZCY-Co_x and the microstructure of R-BZCY-Co_x||BCZY||R-BZCY-Co_x symmetric half-cells were observed using a high-resolution transmission electron microscope (HRTEM, FEI Tecnai F30 TWIN) and a field-emission scanning electron microscope (FESEM, Zeiss GeminiSEM 500), respectively. The TECs of electrolyte and electrode were measured ranging from 30 to 1000 °C at a heating rate of 5 °C min^{-1} in air using a PCY-G precision dilatometer (Xiangtan Xiangyi Instrument). For the TEC test, approximately 2.5 g powder was pressed in a stainless-steel module of dimension 25 mm × 8 mm, and the sintered rod (about 21 mm in length, 7 mm in width and 3 mm in thickness) was obtained after sintering at 1500 °C for 10 h. The oxygen vacancies and valence state of the elements were analysed using an X-ray photoelectron spectrometer (XPS, Thermo Scientific K-Alpha+) equipped with an Al Kα radiation source at 1486.6 eV. The XPS data were calibrated as referenced to the C 1s peak at 284.6 eV.

3 Results and discussions

3.1 Physical property characterization

Fig. 1(a) shows the XRD patterns of R-BCZY-Co_x (x = 0.025, 0.05, 0.075, 0.10, 0.15 and 0.20) samples, and those of BCZY-Co_x samples are presented in Fig. S1.† All the BCZY-Co_x and R-BCZY-Co_x powders demonstrate the rhombohedral structure, matching well with the $BaCe_{0.8}Zr_{0.2}O_3$ perovskite (PDF#70-3670). Meanwhile, a small amount of $BaZrO_3$ impurity (PDF#74-1299) could be detected on BCZY-$Co_{0.15}$ and BCZY-$Co_{0.20}$, as shown in Fig. S1(b).† The relative intensity of impurity raises with the increase in Co-doping amount, suggesting that the existence of impurity is closely related to Co incorporation. However, such $BaZrO_3$ phase disappears on R-BCZY-$Co_{0.15}$ and R-BCZY-$Co_{0.20}$ after the reduction treatment (at 800 °C for 10 h in an atmosphere containing 5% H_2/N_2), which could be explained by the possible dissolution of $BaZrO_3$ in the main perovskite phase after reduction.[32,33] Table S1† lists the calculated tolerance factors of BCZY-Co_x samples, which are in the range of 0.960–0.986. All the values are close to 1, meeting the tolerance limit of perovskite phase. What is more, the R-BCZY-Co_x powders show the maintenance of the perovskite phase with the co-existence of metallic Co phase at 2θ = ~ 44.2° (PDF#15-0806).[34] The amount of exsolved Co NPs is proportional to the Co-doping level, as shown in Fig. 1(b). This result preliminarily proves the successful Co metal exsolution on the surface of R-BCZY-Co_x. Fig. 1(c) exhibits the HRTEM images of R-BCZY-$Co_{0.10}$. The measured lattice spacing is ~0.306 nm, matching well with the lattice spacing of the (111) plane (~0.307 nm) calculated by the XRD pattern of R-BCZY-$Co_{0.10}$ with the diffraction peak at 2θ = ~29.06° based on Bragg's law (λ = 0.15406 nm). It further confirms the maintenance of perovskite structure after the reduction treatment.

Furthermore, the H_2-TPR measurement was employed to investigate the reducibility of BCZY-Co_x with pure BCZY as a reference. It can be seen from Fig. 1(d) that the weak H_2 consumption peaks at ~600 and ~730 °C are ascribed to the reduction of Ce^{4+} to Ce^{3+} in BCZY, which is in agreement with the result reported by He *et al.*[35] For BCZY-Co_x (x = 0.025, 0.05, 0.075, 0.10, 0.15 and 0.20) samples, there are two extra H_2 consumption peaks at 360–400 and 420–470 °C, which are related

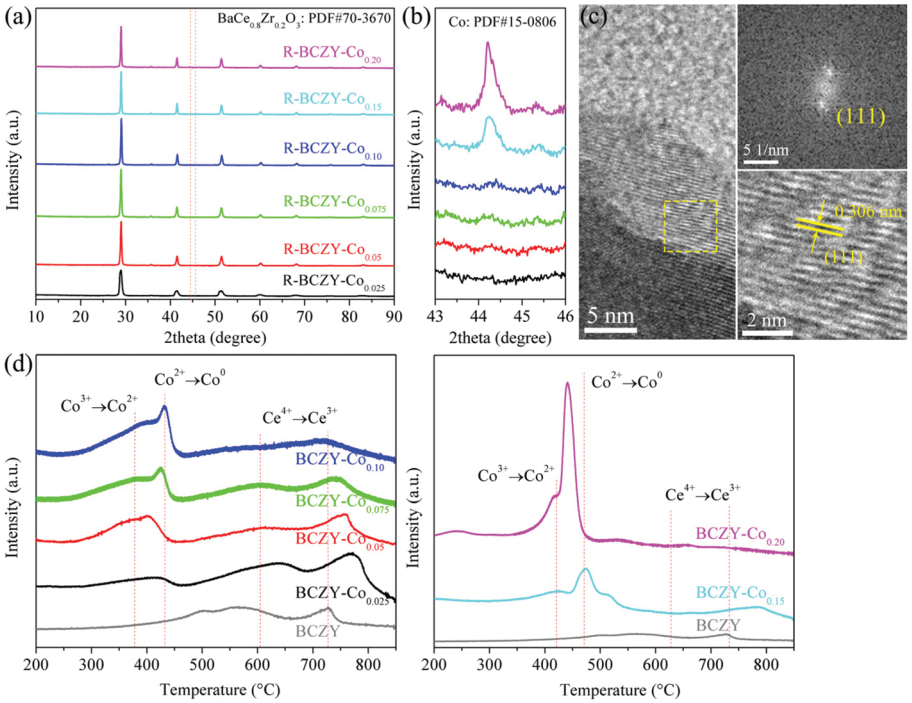

Fig. 1 (a) XRD patterns of R-BCZY-Co$_x$ (x = 0.025, 0.05, 0.075, 0.10, 0.15 and 0.20) powders. (b) Slow step scan XRD patterns ranging from 43° to 46° in (a). (c) HRTEM images of R-BCZY-Co$_{0.10}$. (d) H_2-TPR curves of BCZY-Co$_x$.

to the reduction of Co^{3+} to Co^{2+} and Co^{2+} to Co^0, respectively.[36,37] As the Co-doping amount increases, the reduction peak areas become greater, indicating that a larger amount of Co with high valence state are reduced. Based on the H_2-TPR results, it is concluded that the condition of 800 °C for 10 h in an atmosphere containing 5% H_2/N_2 is sufficient to trigger the reduction of Co ions and the exsolution of Co NPs.

Fig. S2† provides the morphological information of all the R-BZCY-Co$_x$ samples. As illustrated by the example of R-BCZY-Co$_{0.10}$ (Fig. 2(a) and Fig. S2(a–f)†), the widely dispersed pinned Co NPs are clearly observed on all the surface of reduced samples and the particle sizes are in the range of 30–100 nm. The amount of Co NPs on R-BZCY-Co$_{0.025}$ is small as compared to the other counterparts, which can be explained by its trace Co-doping amount. The Co 2p XPS spectra of samples before/after reduction are shown in Fig. 2(b) and Fig. S3.† The Co $2p_{3/2}$ peaks located at ~779.5 and ~781.9 eV are assigned to Co^{3+} and Co^{2+}, respectively. While an additional small Co $2p_{3/2}$ peak appears at ~777.0 eV for the reduced sample, suggesting the appearance of Co^0, which is in agreement with the results reported in literatures for Co exsolution.[38,39] The TEM and HAADF-STEM images and the corresponding EDS elemental mappings of R-BCZY-Co$_{0.10}$ shown in Fig. 2(c) further corroborate the emergence of metallic Co NPs. Apparently, the Ba, Ce, Zr, Y, O and Co species are evenly dispersed well on the bulk of R-BCZY-Co$_{0.10}$, with bright spots on Co mapping only.

Fig. 3(a) presents the thermal expansion curves and TECs of BCZY electrolytes and BCZY-Co$_x$ electrodes measured ranging from 200 to 1000 °C in air. The average TEC of BCZY is measured to be ~9.6 × 10^{-6} K^{-1}, which is close to ~10.2 × 10^{-6} K^{-1} of BZCY[40] and ~9.5 × 10^{-6} K^{-1} of BCZYYb.[3] The average TECs of BCZY-Co$_x$ are in the range of ~10.2–11.4 × 10^{-6} K^{-1}, leading to the calculated discrepancy of TECs between the electrolyte and the electrode to be ~0.7–1.9 × 10^{-6} K^{-1}. This result is much smaller than 7.0 × 10^{-6} K^{-1}, the reported threshold for interface delamination.[14] Fig. 3(b) summarizes the reported TECs of electrolytes and Co-based electrodes in literatures.[1,3,11,12,40–52] Generally, the TECs of typical SOC electrolytes are in the range of 9–13 × 10^{-6} K^{-1}, significantly smaller than 15–24 × 10^{-6} K^{-1} of Co-based electrodes. The huge differences of TECs are in the range of 5–12 × 10^{-6} K^{-1}, leading to the risk of thermal-mechanical instability. The calculated TEC mismatches between representative electrolytes and electrodes are further presented in Fig. 3(c).[1,11,44–46,49,50,53] It can be seen that the TEC mismatches shown in our work are all below 20% and the minimum one is even as low as ~6.2%. While the TEC mismatches reported in literatures are generally above 50% with the smallest value of ~26% between the $YBaCo_2O_{5+\delta}$ electrode and the $Gd_{0.1}Ge_{0.9}O_{1.95}$ electrolyte.[50] Hence, the negligible TEC mismatch reported in our work ensures a good contact between electrode and electrolyte for future long-term operation.

3.2 Electrocatalytic performance

Fig. S4† shows the cross-sectional microstructure of R-BCZY-Co$_{0.10}$||BCZY||R-BCZY-Co$_{0.10}$ symmetrical half-cell and

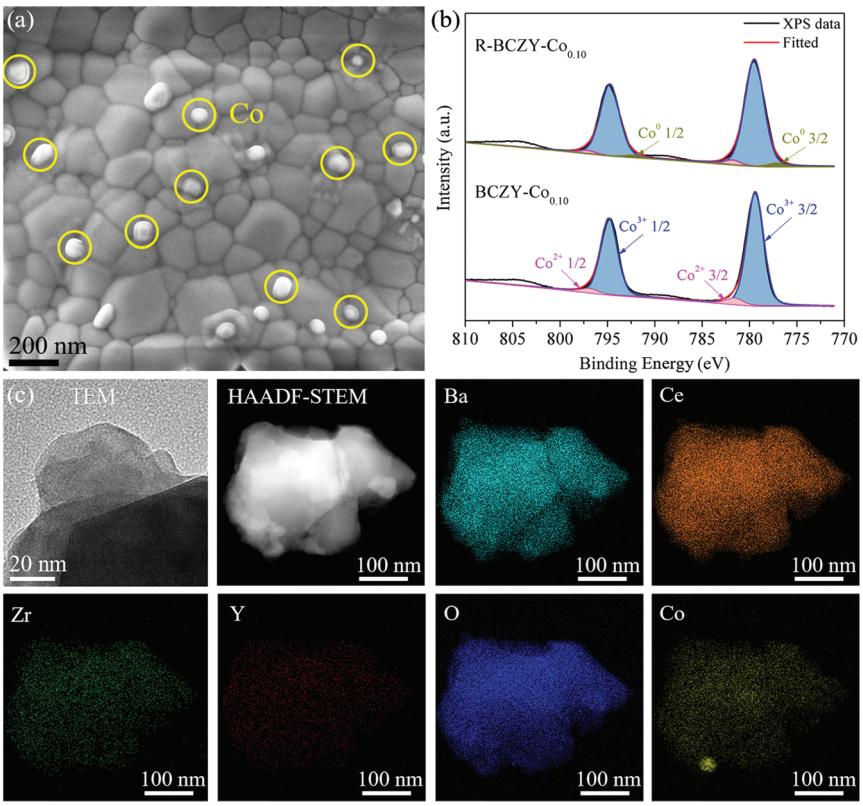

Fig. 2 (a) SEM image of the R-BCZY-$Co_{0.10}$ powder. (b) High-resolution XPS spectra of Co 2p on the surfaces of BCZY-$Co_{0.10}$ and R-BCZY-$Co_{0.10}$. (c) TEM, STEM-HAADF and EDS images of R-BCZY-$Co_{0.10}$. The EDS elemental mappings of Ba, Ce, Zr, Y, O and Co are represented in cyan, orange, green, red, blue and yellow, respectively.

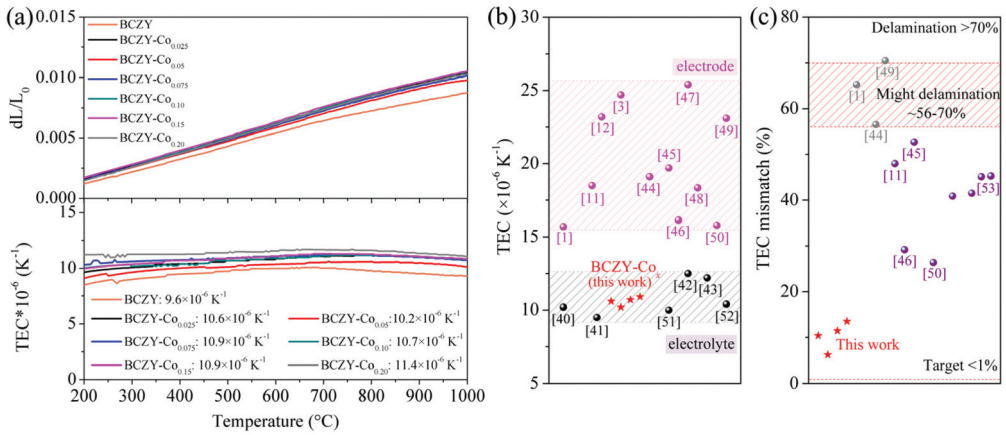

Fig. 3 (a) Thermal expansion (dL/L_0) curves and TEC values of the BCZY electrolyte and BCZY-Co_x electrodes in the temperature range of 200–1000 °C in air. (b) Summary of TECs of representative electrodes and electrolytes reported in the literature. (c) Calculated TEC mismatches between reported electrolytes and electrodes. The numbers in (b) and (c) correspond to the number of literatures in references. Tables S2 and S3† list the electrolytes and Co-based electrodes in (b) and (c), respectively.

the morphology of R-BCZY-$Co_{0.10}$ air electrode before/after the EIS test, where the cell was tested at 750–550 °C with an interval of 50 °C in air. Obviously, the BCZY electrolyte is dense and its thickness is approximately 450 μm, as shown in Fig. S4(a).† The R-BCZY-$Co_{0.10}$ electrode layer with a thickness of ~20 μm is attached well to the surface of BCZY. Fig. S4(b) and (c)† present the morphology of the R-BCZY-$Co_{0.10}$ electrode before and after the EIS test, respectively. A large number of circular Co NPs are exsolved on the surface of a fresh electrode layer. After the EIS test, the polygonal Co NPs

are still observed on the surface of electrode layer, manifesting that the Co reactive centres can be preserved well during measurement. The morphology change could be probably ascribed to the phase transformation of metallic Co to CoO_x under oxidative testing condition.[54]

The electrochemical performance of R-BCZY-Co_x||BCZY||R-BCZY-Co_x symmetric half-cells was tested at an elevated temperature in air, and all the EIS data were analysed by an equivalent circuit model. The representative fitting EIS results of R-BCZY-$Co_{0.10}$||BCZY||R-BCZY-$Co_{0.10}$ at 650 °C in air are shown in Fig. 4(a). This model contains four R–Q elements, and the Nyquist and Bode plots are divided into four parts corresponding to high frequency (HF), middle frequency (MF1 and MF2) and low frequency (LF). The fitting results exhibit a good match with the experimental data.

Fig. S5† shows the electrochemical performance of BCZY||BCZY||BCZY symmetric half-cell at 750–550 °C in air. It is found that the total polarization resistance (R_p) of BCZY symmetric cell is as high as ~1.2, ~3.5 and ~7.2 Ω cm^2 at 750, 700 and 650 °C, respectively, indicating the catalytically inert property of BCZY. Fig. 4(b) illustrates the EIS results of R-BCZY-$Co_{0.10}$||BCZY||R-BCZY-$Co_{0.10}$ and BCZY-$Co_{0.10}$||BCZY||BCZY-$Co_{0.10}$ cells at different temperatures. The R_p value of the R-BCZY-$Co_{0.10}$ symmetric cell measured at 750 °C was determined to be ~0.17 Ω cm^2, which is ~30% smaller than ~0.23 Ω cm^2 of the BCZY-$Co_{0.10}$ symmetric cell, and even only 1/7 of that of the BCZY symmetric cell. Excitingly, this value is comparable to other representative Co-based perovskite electrodes reported in literatures,[14,45,55–61] as listed in Table 1. The R_p values of R-BCZY-$Co_{0.10}$ symmetric cell measured at 700, 650, 600 and 550 °C are all smaller than those of BCZY-$Co_{0.10}$ symmetric cell (~0.6 *vs.* ~0.7 Ω cm^2 at 700 °C, ~1.5 *vs.* ~2.1 Ω cm^2 at 650 °C, ~4.2 *vs.* ~5.5 Ω cm^2 at 600 °C, and ~11.7 *vs.* ~15.5 Ω cm^2 at 550 °C). Thereby, it can be inferred that the Co incorporation significantly reduces the polarization resistance of cells, and surface segregation Co sites could serve as the effective reaction centres for oxygen activation. Fig. S6† presents the evolution of polarization resistance including $R_{p,HF}$, $R_{p,MF1}$, $R_{p,MF2}$ and $R_{p,LF}$ in Fig. 4(b). All the resistances increase with the decrease in temperature, and $R_{p,HF}$ is the dominant polarization resistance at a temperature of 600–750 °C, but it occupies the smallest portion at 550 °C.

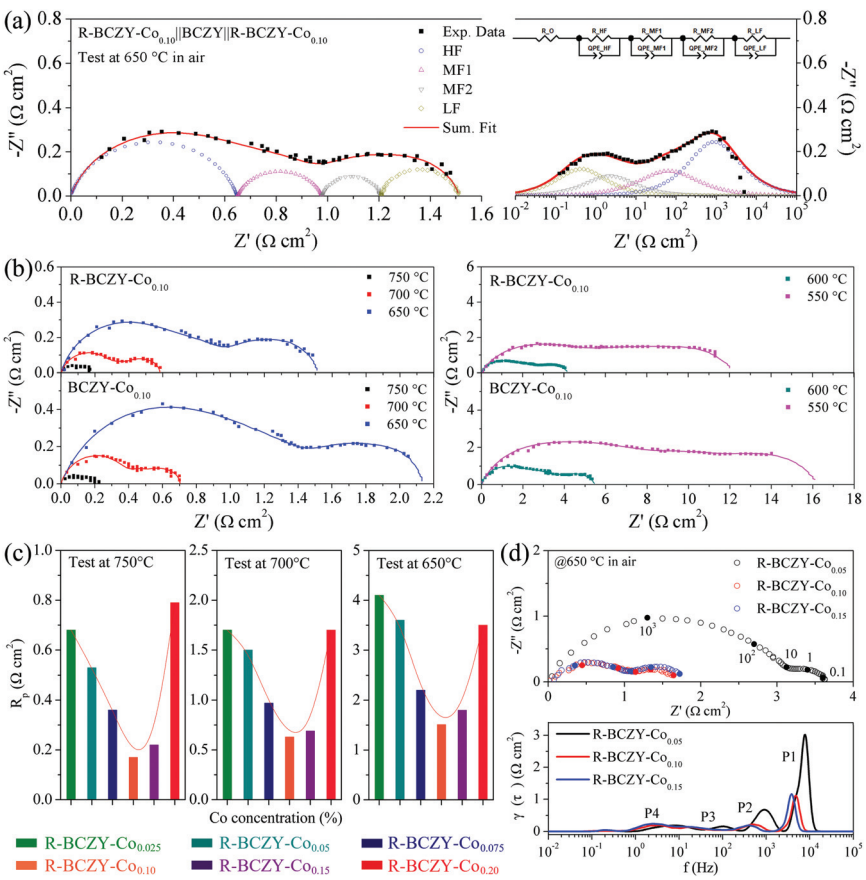

Fig. 4 (a) EIS fitting result using an equivalent circuit model of R-BCZY-$Co_{0.10}$|| BCZY||R-BCZY-$Co_{0.10}$ at 650 °C in air under OCV condition. (b) EIS results of R-BCZY-$Co_{0.10}$||BCZY||R-BCZY-$Co_{0.10}$ and BCZY-$Co_{0.10}$||BCZY||BCZY-$Co_{0.10}$ cells measured at 750 to 550 °C in air under OCV condition. (c) Polarization resistances of R-BCZY-Co_x||BCZY||R-BCZY-Co_x (x = 0.025, 0.05, 0.075, 0.10, 0.15 and 0.20) cells measured at 750 °C, 700 °C and 650 °C, respectively. (d) EIS results and the corresponding DRT plots of R-BCZY-Co_x||BCZY||R-BCZY-Co_x (x = 0.05, 0.10 and 0.15) cells at 650 °C in air under OCV conditions. The solid lines in (b) and (c) are the fitting results. All the ohmic resistances were subtracted for clear comparison.

Table 1 Polarization resistances of some Co-based electrodes for SOC in the literature

Electrodes	Electrolytes	R_p (Ω cm^2) 750 °C	700 °C	Ref.
R-BCZY-$Co_{0.10}$	BCZY	0.17	0.60	This work
$La_{0.6}Sr_{0.4}Co_{0.2}Fe_{0.8}O_{3-\delta}$	BCZYYb	—	1.1	55
$Ba_{0.5}Sr_{0.5}Co_{0.8}Fe_{0.2}O_{3-\delta}$	GDC	—	0.04	56
$BaFe_{0.125}Co_{0.125}Zr_{0.75}O_{3-\delta}$	GDC	0.22	0.33	14
$(Pr_{0.6}Sr_{0.4})_{0.99}Co_{0.2}Fe_{0.8}O_{3-\delta}$	GDC	—	1.6	45
$(Sm_{0.6}Sr_{0.4})_{0.99}Co_{0.2}Fe_{0.8}O_{3-\delta}$	GDC	—	0.50	45
$SrCoO_{3-\delta}$	LSGM	—	4.1	57
$SrCo_{0.8}Fe_{0.2}O_{3-\delta}$	LSGM	—	2.5	58
$Ca_3Co_2O_6$	LSGM	0.25	0.51	59
$SmBaCo_{1.45}Mn_{0.5}Mg_{0.05}O_{5+\delta}$	SDC	0.40	0.77	60
$SmBaCo_{0.4}Mn_{1.5}Mg_{0.1}O_{5+\delta}$	SDC	0.65	1.5	60
$PrBa_{0.5}Sr_{0.5}Co_{1.5}Fe_{0.5}O_{5+\delta}$	YSZ	0.03	0.04	61

Fig. S7† provides the Co content–dependent EIS results of R-BCZY-Co_x||BCZY||R-BCZY-Co_x (x = 0.025, 0.05, 0.075, 0.10, 0.15 and 0.20) symmetric half-cells. The R_p values of each R-BCZY-Co_x symmetric cell at 750, 700 and 650 °C are summarized in Fig. 4(c) and those at 600 and 550 °C are provided in Fig. S8.† There exists an inverted volcanic relationship between the Co-doping amount and the R_p value of symmetric cells, and 10 mol% is determined to be the optimal Co doping level. As illustrated by the example of cells at 650 °C, the R_p value of R-BCZY-$Co_{0.10}$ symmetric cell is ~1.7 Ω cm^2. Decreasing the Co-doping amount leads to an increase in the R_p value to ~4.1 Ω cm^2 for R-BCZY-$Co_{0.025}$ symmetric cell, probably due to the less amount of Co active sites (confirmed by SEM images shown in Fig. S2(a)† and XRD patterns shown in Fig. 1(b)), while further boosting the Co-doping amount also rises the R_p value to ~3.2 Ω cm^2 for R-BCZY-$Co_{0.20}$ symmetric cell.

To investigate the electrochemical processes on R-BCZY-Co_x in detail, the EIS plots were further analysed by the distribution of relaxation time (DRT) method. The DRT data were calculated using the MATLAB program (named DRTtools) developed by Ciucci group.[62] Fig. 4(d) shows the EIS results and the corresponding DRT plots of R-BCZY-$Co_{0.05}$, R-BCZY-$Co_{0.10}$ and R-BCZY-$Co_{0.15}$ symmetric cells at 650 °C in air. The operating temperature–dependent (750–550 °C) DRT plots of R-BCZY-$Co_{0.10}$ symmetric cell are shown in Fig. S9.† All the DRT plots are deconvoluted into four typical peaks (denoted as P1–P4) in the frequency range of 10^{-2}–10^5 Hz. According to the previous literatures,[63,64] these four electrode reaction processes can be identified as follows. The P4 peak located in the low frequency range of 1–10 Hz is commonly assigned to the gas diffusion process in porous R-BCZY-Co_x electrode. The intermediate-frequency of P3 (10–10^2 Hz) and P2 (10^2–10^3 Hz) are associated with chemical surface exchange of O_2 and O^{2-} bulk diffusion, respectively. The P1 at high frequency (10^3–10^4 Hz) is ascribed to the charge transfer process. The proportions of different frequency bands (*i.e.*, P1–P4 peaks) were calculated, and are presented in Fig. S10 and S11.† Obviously, the proportion of P1 is greater than those of the other three peaks for different Co-doping amounts as well as at 750–600 °C, evidencing that the surface charge transfer process is the rate-limiting step for R-BCZY-Co_x symmetric cells. When the temperature decreases to 550 °C, the gas diffusion process becomes the rate-limiting step.

3.3 Further discussion

To further explore other intrinsic reason for the advanced electrocatalytic performance of R-BCZY-Co_x, the electronic configuration and total conductivities of various materials were analysed. Fig. 5(a) shows the O 1s XPS spectra of BCZY-$Co_{0.10}$ and R-BCZY-$Co_{0.10}$. The high-resolution O 1s spectra are deconvoluted into four peaks, namely, lattice oxygen species (O_I, O^{2-} at ~528.6 eV), highly oxidative oxygen species (O_{II}, O_2^{2-}/O^- at ~530.3 eV), hydroxyl groups or surface-adsorbed oxygen (O_{III}, –OH or O_2 at ~531.5 eV), and surface-adsorbed water (O_{IV}, H_2O at ~532.9 eV).[65,66] The relative proportions of four oxygen species (*i.e.*, O_I, O_{II}, O_{III} and O_{IV}) were calculated by the area of fitted subpeaks. Among these oxygen species, O_{II} and O_{III} are recognized to be related to oxygen vacancies.[65] The area ratio of (O_{II} + O_{III}/O_I + O_{II} + O_{III} + O_{IV}) on R-BCZY-$Co_{0.10}$ is calculated to be ~88.7%, which is greater than that of BCZY-$Co_{0.10}$ (~69.3%). Fig. 5(b) shows the Co content–dependent O 1s XPS spectra. The area ratio of (O_{II} + O_{III}/O_I + O_{II} + O_{III} + O_{IV}) on R-BCZY-$Co_{0.05}$ (~65.7%) is much smaller than that of R-BCZY-$Co_{0.10}$ (~88.7%) and that of R-BCZY-$Co_{0.15}$ (~86.0%), suggesting its less surface vacancy sites for oxygen absorption/activation. This result is consistent with the DRT data shown in Fig. 4(d) that R-BCZY-$Co_{0.05}$ has much greater P3 and P2 peak areas ascribed to more reluctant surface oxygen exchange kinetics. Therefore, it is concluded that the Co exsolution not only provides sufficient reactive sites, but also grants higher concentrations of oxygen vacancy, which is beneficial to ionic diffusion and oxygen absorption.

As discussed in Fig. 4(d), the surface charge transfer process is the rate-determining step for R-BCZY-Co_x symmetric cells, manifesting that the electrical conduction could be a crucial parameter for future material optimization. Fig. 5(c) presents the total conductivities of BCZY-$Co_{0.10}$ and R-BCZY-Co_x (x = 0.05, 0.10 and 0.15), which were measured in air ranging from 400 to 850 °C. It can be seen that all the Co-

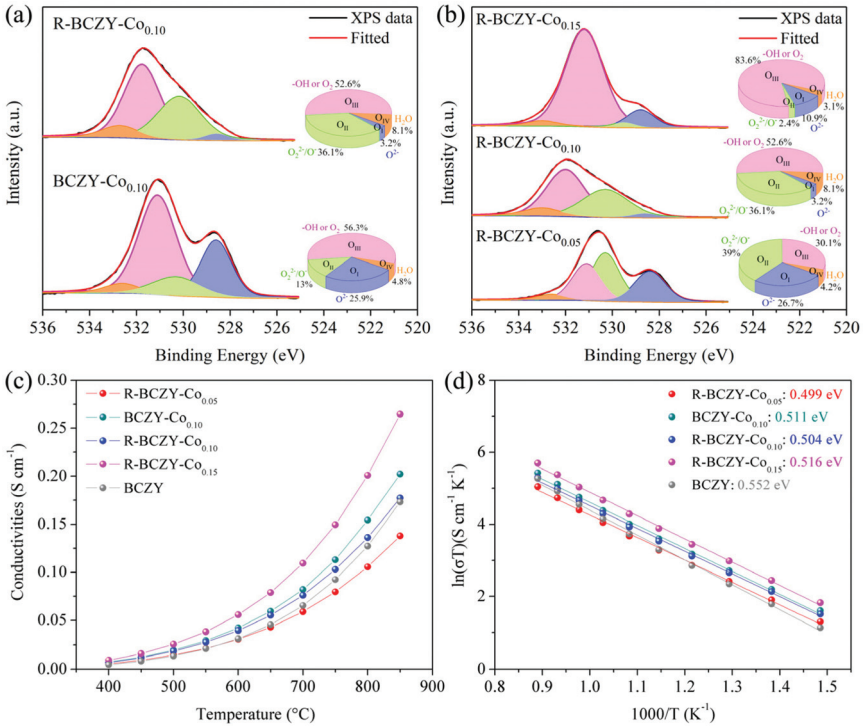

Fig. 5 High-resolution XPS spectra of O 1s and the calculated relative proportion of different oxygen species on the surface of (a) BCZY-$Co_{0.10}$ and R-BCZY-$Co_{0.10}$, and (b) R-BCZY-$Co_{0.05}$, R-BCZY-$Co_{0.10}$ and R-BCZY-$Co_{0.15}$. (c) Total conductivities in air of BCZY, BCZY-Co_x and R-BCZY-Co_x (x = 0.05, 0.10 and 0.20). (d) Corresponding Arrhenius plots of $\ln(\sigma T)$ *vs.* $1000/T$.

containing samples display a typical p-type semi-conductor behaviour.[1] The measured conductivities gradually increase with the increase of temperature, indicative of the small polaron hopping mechanism.[10] The conductivity of BCZY-$Co_{0.10}$ is observed to be slightly greater than that of R-BCZY-$Co_{0.10}$ (*e.g.*, ~0.042 *vs.* ~0.040 S cm^{-1} at 600 °C, ~0.082 *vs.* ~0.076 S cm^{-1} at 700 °C, and ~0.15 *vs.* ~0.14 S cm^{-1} at 800 °C). The decrease in the conductivity of R-BCZY-$Co_{0.10}$ might be due to the introduction of oxygen vacancy after the reduction treatment.[67] Furthermore, the conductivities of R-BCZY-Co_x at a certain temperature increase with the increase of Co-doping amount. For example, the conductivity of R-BCZY-$Co_{0.05}$ at 650 °C is ~0.04 S cm^{-1}, and those of R-BCZY-$Co_{0.10}$ and R-BCZY-$Co_{0.15}$ increase to ~0.06 and ~0.08 S cm^{-1}, respectively. This can be explained by the contribution of surface Co species for enhancing the electronic conductivity. The lower conductivity of R-BCZY-$Co_{0.05}$ than those of R-BCZY-$Co_{0.10}$ and R-BCZY-$Co_{0.15}$ is consistent with the greater P1 peak area of R-BCZY-$Co_{0.05}$ symmetric cell, as presented in Fig. 4(d).

The conductivity of BCZY was also evaluated by the van der Pauw DC conductivity test and the BCZY slurry was screen-printed on one side of BCZY electrolyte. However, there is no pronounced difference in conductivity between BCZY and Co-doped samples, as shown in Fig. 5(c), which fails to explain the observation that the R_p value of BCZY is 7-fold greater than that of R-BCZY-Co_x. Thereby, it is concluded that the improvement of electrochemical performance for R-BCZY-Co_x is mainly related to the introduction of Co as active sites rather than the conductivity.

Fig. 5(d) shows the corresponding Arrhenius plots of $\ln(\sigma T)$ *vs.* $1000/T$ for these samples in air. According to the Arrhenius equation, the activation energies for electrical conduction were calculated by the slopes of the fitted lines. The activation energy for conductivity of BCZY was measured to be ~0.552 eV. In comparison, the activation energies for the conductivity of BCZY-$Co_{0.10}$ and R-BCZY-Co_x (x = 0.05, 0.10 and 0.15) are in the range of ~0.50–0.52 eV. which are the typical values for proton transport (0.3–0.6 eV).[3] The activation energies for conductivity in this work are close to ~0.44 eV of $BaCe_{0.7}Zr_{0.1}Y_{0.1}Co_{0.1}O_{3-\delta}$ and ~0.59 eV of $BaCe_{0.7}Zr_{0.1}Y_{0.18}Co_{0.02}O_{3-\delta}$ reported by Yang *et al.*[68]

Assisted by the design principle of *in situ* exsolution, the direct growth of nano Co active sites onto the BCZY matrix (Fig. 1 and 2) could effectively break through the bottleneck of TEC mismatch (Fig. 3) without the trade-off of electrocatalytic performance (Fig. 4) and system simplicity. However, the ionic-conducting active/electronic-conducting inactive properties of BCZY scaffold still restrict the establishment of fast electrical conduction pathway for electron transfer, which, unfortunately, is unable to be concurrently alleviated by the exsolved nanoparticles with isolated-standing modality (Fig. 5). In future work, other strategies that could boost the electronic conduction of the materials without sacrificing other merits should be pursued.

4 Conclusions

In this work, a series of *in situ* exsolved Co-decorated Ba$(Ce_{0.7}Zr_{0.2}Y_{0.1})_{1-x}Co_xO_{3-\delta}$ perovskites (x = 0.025, 0.05, 0.075, 0.10, 0.15 and 0.20) have been synthesized by the sol–gel method. Multiple types of characterization including XRD, H_2-TPR, XPS, SEM and EDS mapping confirm the exsolved Co NPs on the surface of R-BCZY-Co_x after reduction. Results of TEC test show that the average TECs of BCZY-Co_x are in the range of ~10.2–11.4 × 10^{-6} K^{-1}, which are very close to that of the as-synthesized BCZY (~9.6 × 10^{-6} K^{-1}) electrolyte and can eliminate the risk of electrode/electrolyte interface delamination. The EIS results of symmetric half-cells indicate that there exists an inverted volcanic shape relationship between the Co-doping amount and electrochemical performance, and Co exsolution significantly reduced the R_p value by up to 7-fold. The promoted performance is not only due to the formation of Co reactive centres, but also owing to the enhanced concentration of oxygen vacancies in R-BCZY-Co_x. We believe this facile design paradigm is universally practical for many other SOC systems.

Author contributions

Zhishan Li: Data curation, investigation, formal analysis, methodology, writing-original draft. Meilan Peng: Data curation, formal analysis. Yingru Zhao: Funding acquisition, project administration, writing-review & editing. Jianhui Li: Funding acquisition, resources, writing-review & editing. Yifei Sun: Conceptualization, funding acquisition, supervision, writing-review & editing.

Conflicts of interest

There are no conflicts to declare.

Acknowledgements

Y. Sun thanks Guangdong Basic and Applied Basic Research Foundation (2020A1515110904) for the financial support. This work is also supported by the National Natural Science Foundation of China (No. 22102135, 22172129, 21773195) and the Natural Science Foundation of Fujian Province of China (2021J05014).

References

1 Y. Song, Y. Chen, W. Wang, C. Zhou, Y. Zhong, G. Yang, W. Zhou, M. Liu and Z. Shao, *Joule*, 2019, **3**, 2842–2853.
2 L. Chen, F. Chen and C. Xia, *Energy Environ. Sci.*, 2014, **7**, 4018–4022.
3 J.-S. Shin, H. Park, K. Park, M. Saqib, M. Jo, J. H. Kim, H.-T. Lim, M. Kim, J. Kim and J.-Y. Park, *J. Mater. Chem.*, 2021, **9**, 607–621.
4 X. Zhang, J. Zhou and Y. Wang, *Ionics*, 2013, **19**, 941–945.
5 D.-K. Lim, J.-H. Kim, A. U. Chavan, T.-R. Lee, Y.-S. Yoo and S.-J. Song, *Ceram. Int.*, 2016, **42**, 3776–3785.
6 L. dos Santos-Gómez, S. Sanna, P. Norby, N. Pryds, E. R. Losilla, D. Marrero-López and V. Esposito, *Nanoscale*, 2019, **11**, 2916–2924.
7 C. Duan, J. Tong, M. Shang, S. Nikodemski, M. Sanders, S. Ricote, A. Almansoori and R. O'Hayre, *Science*, 2015, **349**, 1321–1326.
8 Y. Niu, Y. Zhou, W. Lv, Y. Chen, Y. Zhang, W. Zhang, Z. Luo, N. Kane, Y. Ding, L. Soule, Y. Liu, W. He and M. Liu, *Adv. Funct. Mater.*, 2021, **31**, 2100034.
9 Y. Zhang, B. Chen, D. Guan, M. Xu, R. Ran, M. Ni, W. Zhou, R. O'Hayre and Z. Shao, *Nature*, 2021, **591**, 246–251.
10 Y. Chen, Q. Gu, D. Tian, Y. Ding, X. Lu, W. Yu, T. T. Isimjan and B. Lin, *Int. J. Hydrogen Energy*, 2014, **39**, 13665–13670.
11 A. Petric, P. Huang and F. Tietz, *Solid State Ionics*, 2000, **135**, 719–725.
12 A. S. Harvey, F. J. Litterst, Z. Yang, J. L. M. Rupp, A. Infortuna and L. J. Gauckler, *Phys. Chem. Chem. Phys.*, 2009, **11**, 3090–3098.
13 J. Liang, R. Sazinas and K. K. Hansen, *Ceram. Int.*, 2021, **47**, 5407–5414.
14 E. Sánchez-Ahijón, R. Marín-Gamero, B. Molero-Sánchez, D. Ávila-Brande, A. Manjón-Sanz, M. T. Fernández-Díaz, E. Morán, R. Schmidt and J. Prado-Gonjal, *J. Mater. Chem.*, 2020, **8**, 3413–3420.
15 S. Lee, I. Park, H. Lee and D. Shin, *Int. J. Hydrogen Energy*, 2014, **39**, 14342–14348.
16 L. Gui, Y. Ling, G. Li, Z. Wang, Y. Wan, R. Wang, B. He and L. Zhao, *J. Power Sources*, 2016, **301**, 369–375.
17 T. Yang, A. Shaula, D. Pukazhselvan, D. Ramasamy, J. Deng, E. L. da Silva, R. Duarte and J. A. Saraiva, *Appl. Surf. Sci.*, 2017, **424**, 82–86.
18 W. Zhou, R. Ran, Z. Shao, W. Jin and N. Xu, *J. Power Sources*, 2008, **182**, 24–31.
19 Y. Song, Y. Chen, M. Xu, W. Wang, Y. Zhang, G. Yang, R. Ran, W. Zhou and Z. Shao, *Adv. Mater.*, 2020, **32**, 1906979.
20 Y. Sun, J. Li, Y. Zeng, B. S. Amirkhiz, M. Wang, Y. Behnamian and J. Luo, *J. Mater. Chem.*, 2015, **3**, 11048–11056.
21 Y. Sun, Y. Zhang, J. Chen, J. Li, Y. Zhu, Y. Zeng, B. S. Amirkhiz, J. Li, B. Hua and J. Luo, *Nano Lett.*, 2016, **16**, 5303–5309.
22 B. Hua, M. Li, Y. F. Sun, J. H. Li and J. L. Luo, *ChemSusChem*, 2017, **10**, 3333–3341.
23 X. Chen, W. Ni, J. Wang, Q. Zhong, M. Han and T. Zhu, *Electrochim. Acta*, 2018, **277**, 226–234.
24 U. Anjum, M. Agarwal, T. S. Khan, Prateek, R. K. Gupta and M. A. Haider, *Nanoscale*, 2019, **11**, 21404–21418.
25 X. Sun, H. Chen, Y. Yin, M. T. Curnan and Z. Ma, *Small*, 2021, **17**, e2005383.

26 Y. Wan, B. He, R. Wang, Y. Ling and L. Zhao, *J. Power Sources*, 2017, **347**, 14–20.
27 Y. Liu, L. Jia, B. Chi, J. Pu and J. Li, *ACS Omega*, 2019, **4**, 21494–21499.
28 J. Tong, D. Clark, M. Hoban and R. O'Hayre, *Solid State Ionics*, 2010, **181**, 496–503.
29 T. Zhu, X. Chen, W. Ni, Q. Zhong and M. Han, *Int. J. Hydrogen Energy*, 2019, **44**, 31386–31393.
30 W. Ni, T. Zhu, X. Chen, Q. Zhong and W. Ma, *J. Power Sources*, 2020, **451**, 227762.
31 A. Esquirol, N. P. Brandon, J. A. Kilner and M. Mogensen, *J. Electrochem. Soc.*, 2004, **151**, A1847–A1855.
32 K. Katahira, Y. Kohchi, T. Shimura and H. Iwahara, *Solid State Ionics*, 2000, **138**, 91–98.
33 S. Wang, F. Zhao, L. Zhang and F. Chen, *Solid State Ionics*, 2012, **213**, 29–35.
34 C. Xu, W. Sun, R. Ren, X. Yang, M. Ma, J. Qiao, Z. Wang, S. Zhen and K. Sun, *Appl. Catal., B*, 2021, **282**, 119553.
35 F. He, Q. Gao, Z. Liu, M. Yang, R. Ran, G. Yang, W. Wang, W. Zhou and Z. Shao, *Adv. Energy Mater.*, 2021, **11**, 2003916.
36 M. Zhao, J. Deng, J. Liu, Y. Li, J. Liu, Z. Duan, J. Xiong, Z. Zhao, Y. Wei, W. Song and Y. Sun, *ACS Catal.*, 2019, **9**, 7548–7567.
37 S. A. Leonardi, F. E. Tuler, E. M. Gaigneaux, D. P. Debecker, E. E. Miró and V. G. Milt, *Environ. Sci. Pollut. Res.*, 2018, **25**, 35276–35286.
38 Y. Yang, Y. Wang, Z. Yang, Z. Lei, C. Jin, Y. Liu, Y. Wang and S. Peng, *J. Power Sources*, 2019, **438**, 226989.
39 Y. Yang, Y. Wang, Z. Yang, Y. Chen and S. Peng, *J. Power Sources*, 2020, **478**, 229082.
40 Z. Zhu, Z. Tao, L. Bi and W. Liu, *Mater. Res. Bull.*, 2010, **45**, 1771–1774.
41 L. Zhang, S. Yang, S. Zhang and Y. Yang, *Int. J. Hydrogen Energy*, 2019, **44**, 27921–27929.
42 E. V. Tsipis and V. V. Kharton, *J. Solid State Electrochem.*, 2008, **12**, 1039–1060.
43 X. Kong, G. Liu, Z. Yi and X. Ding, *Int. J. Hydrogen Energy*, 2015, **40**, 16477–16483.
44 W. Zhou, W. Jin, Z. Zhu and Z. Shao, *Int. J. Hydrogen Energy*, 2010, **35**, 1356–1366.
45 K. Kammer, *Solid State Ionics*, 2006, **177**, 1047–1051.
46 K. K. Hansen, *Fuel Cells*, 2018, **18**, 96–100.
47 Z. Li, B. Wei, Z. Lü, Y. Zhang, K. Chen, J. Miao and W. Su, *Ceram. Int.*, 2012, **38**, 3039–3046.
48 S. Y. Istomin, O. A. Drozhzhin, P. S. Napolsky, S. N. Putilin, A. A. Gippius and E. V. Antipov, *Solid State Ionics*, 2008, **179**, 1054–1057.
49 T. V. Aksenova, L. Y. Gavrilova, A. A. Yaremchenko, V. A. Cherepanov and V. V. Kharton, *Mater. Res. Bull.*, 2010, **45**, 1288–1292.
50 J. H. Kim and A. Manthiram, *J. Electrochem. Soc.*, 2008, **155**, B385.
51 L. Xu, H. Wang, L. Su, D. Lu, K. Peng and H. Gao, *J. Eur. Ceram. Soc.*, 2021, **41**, 6670–6676.
52 R. Pelosato, G. Cordaro, D. Stucchi, C. Cristiani and G. Dotelli, *J. Power Sources*, 2015, **298**, 46–67.
53 S. Joo, J. Kim, J. Shin, T.-H. Lim and G. Kim, *J. Electrochem. Soc.*, 2016, **163**, F1489–F1495.
54 D. Neagu, E. I. Papaioannou, W. K. W. Ramli, D. N. Miller, B. J. Murdoch, H. Ménard, A. Umar, A. J. Barlow, P. J. Cumpson, J. T. S. Irvine and I. S. Metcalfe, *Nat. Commun.*, 2017, **8**, 1855.
55 J. Gao, Y. Meng, S. Lee, J. Tong and K. S. Brinkman, *JOM*, 2019, **71**, 90–95.
56 S. Lee, Y. Lim, E. A. Lee, H. J. Hwang and J.-W. Moon, *J. Power Sources*, 2006, **157**, 848–854.
57 L. Troncoso, M. C. Gardey, M. T. Fernández-Díaz and J. A. Alonso, *Materials*, 2016, **9**, 717.
58 B. Qu, W. Long, F. Jin, S. Wang and T. He, *Int. J. Hydrogen Energy*, 2014, **39**, 12074–12082.
59 T. Wei, Y.-H. Huang, R. Zeng, L.-X. Yuan, X.-L. Hu, W.-X. Zhang, L. Jiang, J.-Y. Yang and Z.-L. Zhang, *Sci. Rep.*, 2013, **3**, 1125.
60 X. Kong, H. Sun, Z. Yi, B. Wang, G. Zhang and G. Liu, *Ceram. Int.*, 2017, **43**, 13394–13400.
61 C. Gumeci, J. Parrondo, A. M. Hussain, D. Thompson and N. Dale, *Int. J. Hydrogen Energy*, 2021, **46**, 31798–31806.
62 T. H. Wan, M. Saccoccio, C. Chen and F. Ciucci, *Electrochim. Acta*, 2015, **184**, 483–499.
63 T. Zhang, Y. Zhao, X. Zhang, H. Zhang, N. Yu, T. Liu and Y. Wang, *ACS Sustainable Chem. Eng.*, 2019, **7**, 17834–17844.
64 C. Liu, S. Li, J. Gao, L. Bian, Y. Hou, L. Wang, J. Peng, J. Bao, X. Song and S. An, *ACS Appl. Mater. Interfaces*, 2021, **13**, 8229–8238.
65 Y. Zhu, W. Zhou, J. Yu, Y. Chen, M. Liu and Z. Shao, *Chem. Mater.*, 2016, **28**, 1691–1697.
66 Z. Li, L. Cui, J. Luo, J. Li and Y. Sun, *Front. Chem.*, 2021, **8**, 595608.
67 A. Mineshige, J. Izutsu, M. Nakamura, K. Nigaki, J. Abe, M. Kobune, S. Fujii and T. Yazawa, *Solid State Ionics*, 2005, **176**, 1145–1149.
68 L. Yang, S. Wang, X. Lou and M. Liu, *Int. J. Hydrogen Energy*, 2011, **36**, 2266–2270.

